Intercomparison of Fast airborne Ozone Instruments to measure Eddy Covariance Fluxes:

Spatial variability in deposition at the ocean surface and evidence for cloud processing

Randall Chiu[1,2], Florian Obersteiner[3], Alessandro Franchin[4], Teresa Campos[4], Adriana Bailey[4],

Christopher Webster[4], Andreas Zahn[3], and Rainer Volkamer[1,2,*]

1 Department of Chemistry, University of Colorado Boulder, 215 UCB, Boulder, CO, USA

2 Cooperative Institute for Research in Environmental Sciences (CIRES), University of Colorado

Boulder, 216 UCB, Boulder, CO, USA

3 Karlsruhe Institute of Technology, Institute of Meteorology and Climate Research (IMK),

Dept. ASF, Hermann-von-Helmoltz-Platz 1 D-76344 Eggenstine-Leopoldshafen, Germany

4 National Center for Atmospheric Research, P.O. Box 3000, Boulder, CO, 80307, USA

* corresponding authors: randall.chiu@colorado.edu, rainer.volkamer@colorado.edu

Abstract

The air-sea exchange of ozone (O_3) is controlled by chemistry involving halogens, dissolved

organic carbon and sulfur in the sea surface microlayer. Calculations also indicate faster ozone

photolysis at aqueous surfaces, but the role of clouds as ozone sink is currently not well

established. Fast response ozone sensors offer opportunities to measure eddy covariance (EC)

ozone fluxes in the marine boundary layer. However, intercomparisons of fast airborne O_3

sensors, and EC O_3 fluxes measured on aircraft have not been conducted before. In April 2022,

Formatted: Subscript

the ~~TI³GER (~~Technical Innovation Into Iodine and GV aircraft Environmental Research~~)~~ (TI^{3}GER) field campaign deployed three fast ozone sensors (gas chemiluminescence and a combination of UV absorption with coumarin chemiluminescence detection, CID) together with a fast water vapor sensor and anemometer to study iodine chemistry in the troposphere and stratosphere over Colorado and over the Pacific Ocean near Hawaii and Alaska. Here, we present an instrument comparison between the NCAR Fast O3 instrument (FO$_3$, gas-phase CID) and two KIT Fast AIRborne Ozone instruments (FAIRO, UV absorption and coumarin CID). The sensors have comparable precision <0.4% Hz$^{-0.5}$ (0.15 ppbv Hz$^{-0.5}$), and ozone volume mixing ratios (vmr) generally agreed within 2% over a wide range of environmental conditions: $10 < O_3 <$ 1000 ppbv; below detection $< NO_x < 7$ ppbv; and 2 ppmv $< H_2O < 4\%$ VMR. Both instrument designs are demonstrated to be suitable for EC flux measurements and were able to detect O_3 fluxes with exchange velocities (defined as positive for upward) as slow as -0.010 ± 0.004 cm s^{-1}, which is in the lower range of previously reported measurements. Additionally, we present two case studies. In one, the direction of ozone and water vapor fluxes were reversed ($v_{O3} = +0.134 \pm 0.005$ cm s-1), suggesting that overhead evaporating clouds could be a strong ozone sink. Further work is needed to better understand the role of clouds as a possibly widespread sink of ozone in the remote marine boundary layer. In the second case study, v_{O3} are negative (varying by a factor of 6-10 from -0.036 ± 0.006 to -0.003 ± 0.004 cm s^{-1}), while the water vapor fluxes are consistently positive due to evaporation from the ocean surface and spatially homogeneous. This case study demonstrates that the processes governing ozone and water vapor fluxes can become decoupled and illustrates the need to elucidate possible drivers (physical, chemical, or biological) of the variability in ozone exchange velocities on fine spatial scales (~20 km) over remote oceans.

~~Additionally, we present two case studies: one in which the direction of ozone and water vapor~~
~~fluxes were reversed (v_{O3} = +0.134 ± 0.005 cm s^{-1}), suggesting that overhead evaporating clouds~~
~~could be a strong ozone sink; and another in which ozone fluxes v_{O3} are negative (varying by a~~
~~factor of 6-10 from -0.036 ± 0.006 to -0.003 ± 0.004 cm s^{-1}), while the water vapor fluxes are~~
~~consistently positive due to evaporation from the ocean surface and spatially homogeneous.~~
~~Future work is needed to better understand the role of clouds as a possibly widespread sink of~~
~~ozone in the remote marine boundary layer, and to elucidate possible drivers (physical, chemical,~~
~~or biological) of the variability in ozone exchange velocities on fine spatial scales (~20 km) over~~
~~remote oceans.~~

1. Introduction

In the troposphere, ozone is a pollutant with adverse health effects for both animals and plants.
Eddy covariance (EC) is a technique that has been commonly employed to determine the fluxes
of ozone to terrestrial and marine ecosystems. In terrestrial environments, EC flux measurements
have been made over periods of months to years (Bauer et al., 2000; Güsten and Heinrich, 1996).
Over land, uptake to soils and plant stomata are the major sink of ozone (Clifton et al., 2020;
Massman et al., 1995). Consequently, previous campaigns have measured ozone fluxes over a
variety of terrestrial settings including agricultural lands (Lamaud et al., 2009; Massman et al.,
1995; Stella et al., 2011; Zhu et al., 2015, 2020, 2014), forests (Altimir et al., 2006; Fares et al.,
2014; Finco et al., 2017; Juráň et al., 2019; Kammer et al., 2019; Lamaud et al., 2002; Rannik et
al., 2012; Vermeuel et al., 2021; Zeller, 2002; Zeller and Nikolov, 2000), grasslands (Muller et
al., 2009; Wohlfahrt et al., 2009), peatlands (El-Madany et al., 2017), and deserts (Güsten et al.,
1996).

Oceans account for ~1/3 of global ozone dry deposition (Ganzeveld et al., 2009). Ozone losses in the marine environment may be driven by reactions with halogens such as iodide (Saiz-Lopez et al., 2012) or with double bonds from fatty acid precursors (Chiu et al., 2017). EC flux measurements of ozone have also been performed in coastal and oceanic settings (Bariteau et al., 2010; Gallagher et al., 2001; Helmig et al., 2006) and over sea ice (Barten et al., 2023; Muller et al., 2012).

Whereas EC flux measurements of ozone are numerous, comparison studies are fewer. Ozone fluxes from EC methods have been compared to those from gradient measurements (Loubet et al., 2013; Muller et al., 2009; Zhu et al., 2020) and dynamic chamber methods (Plake et al., 2015). Over grassland, Plake et al., (2015) report that dynamic chamber methods agree "well" with EC flux methods (within 11-26%). Over maize fields, Zhu et al., (2020) describe the discrepancy between EC flux and gradient methods as "not very good," with gradient methods measuring ozone fluxes 11.7 – 45.6% higher than those measured by EC flux methods. Furthermore, comparisons of co-located EC flux measurements are uncommon, and complicated due to vertical gradients in the measured fluxes that may explain differences of 10% between measurements on towers (measured by chemiluminescence) and aircraft (measured by a TECO-49) (Massman et al., 1995). To our knowledge, the only aircraft instrument intercomparison for ozone EC flux was performed by Muller et al., (2010), who compared two identical dry chemiluminescence instrumental clones over grassland and found differences up to 12% due to differing sensitivities of chemiluminescent discs. Furthermore, a water sensitivity for chemiluminescent measurement techniques (Ridley et al., 1992) has been suggested to propagate onto EC ozone flux measurements (Boylan et al., 2014), and methods for water correction differ between different methods for measuring ozone. More commonly, a fast ozone instrument is

compared to other ozone instruments only in terms of concentrations (Conley et al., 2011;

90 Hannun et al., 2020). There is currently no intercomparison of different fast ozone instruments that rely on different measurement concepts and respond differently to water sensitivities on research aircraft. Furthermore, the error analysis to estimate EC flux uncertainties is not well developed and is not always treated consistently. This leaves room for instrument and method uncertainty as drivers for overall uncertainty in parameterizing ozone exchange velocities and

95 deposition. Here we eliminate spatial gradients as a source of uncertainty in ozone EC flux intercomparisons by deploying three ozone instruments of two different designs on the same research aircraft in remote marine air. We further use the agreement found among the three sensors to evaluate and refine the EC flux error analysis and define better criteria of use to estimate detection limits.

100 However, comparisons of co-located EC flux measurements are uncommon. Aircraft measurements have been performed near tower facilities (Massman et al., 1995), but ozone fluxes at altitude may differ from those at ground level. To our knowledge, the only aircraft instrument intercomparison for ozone EC flux was performed by Muller et al., (2010), who measured ozone EC flux using two dry chemiluminescence instruments over grassland. The

105 PASE campaign flew two ozone instruments over the equatorial Pacific Ocean, but only one had fast response suitable for EC flux calculation (Conley et al., 2011). Hannun et al., (2020)Here we present the first aircraft ozone EC flux intercomparison of three ozone instruments of two different designs over remote marine air.

Section 2 introduces the Technological Innovation Into Iodine and GV Environmental Research

110 (TI^{3}GER) field campaign, and describes the instruments and methods used to calculate fluxes of

O_3 and H_2O by the EC technique. Section 3 compares the O_3 concentrations and EC fluxes in context with the available literature over oceans, and assesses spatial variability and the EC flux error budget. Finally, Section 4 summarizes the conclusions and gives an outlook for future work.

2. Methods

2.1. The TI^{3}GER field campaign

In April 2022, the Technological Innovation Into Iodine and GV Environmental Research (TI^{3}GER) technical campaign was performed to lay the groundwork for future field investigations into the interactions of ozone and iodine in the upper troposphere lower stratosphere (UTLS). In total, eight research flights (RFs) were conducted, with RFs 01 and 02 over the continental United States, and RFs 03-08 conducted over the Pacific Ocean near Hawaii and Alaska. Among the instruments flown on TI^{3}GER were three ozone instruments, two of which were of an identical design. The NCAR Fast O3 instrument operates by NO_2 chemiluminescence and has been in use since the early 1970s (Pearson, R. and Stedman, 1980; Ridley et al., 1972, 1992; Ridley and Howlett, 1974). Two copies of the Fast AIRborne Ozone (FAIRO) instrument from KIT were also deployed (FAIRO 1 and FAIRO 2). The FAIRO instruments operate by coumarin chemiluminescence calibrated against a dual-beam UV absorption photometer.

One objective of TI^{3}GER was to compare the performance of the two instrument designs and evaluate their ability to measure EC flux of ozone on the NCAR/NSF Gulfstream 5 (GV) platform. The GV measures 3-D winds using a combination of measurements from pitot, static, and radome sensors; the vertical components of these 3-D winds are needed for EC analysis. In

all, EC flux measurements were performed during nineteen legs flown over the Pacific Ocean. The continental flights are not discussed here because they did not include many EC flux measurements. A table of the relevant meteorological and ocean-state variables appears in the supplement as Table S1. Figure 1 shows a map of where attempts were made to measure EC flux. The arrows point to the locations of the flux legs with curves showing the five-day back-trajectories of the sampled air calculated by HYSPLIT (Rolph et al., 2017; Stein et al., 2015) using the National Oceanographic and Atmospheric Administration (NOAA) National Centers for Environmental Prediction (NCEP) Global Forecasting System (GFS) meteorological dataset.

Flux legs were typically 5-10 minutes long. At airspeeds of ~110 m s^{-1}, flux legs covered 30-70 km. A typical flight module consisted of three legs flown in a stacked manner (RF03-B, RF03-C, and RF07-A). However, in the case of RF03-B, fluxes were below detection. Hence, other flight legs were opportunistically used for flux calculations on level legs in the marine boundary layer (MBL). Dedicated flux segments were accompanied by profile descents and ascents.

2.2. Ozone Instrumentation

Three ozone instruments were installed on the GV. Two (the FAIRO instruments) were of an identical design.

2.2.1. The NCAR Fast O3 instrument

The NCAR Fast O3 instrument sampled from a HIAPER Modular Inlet (HIMIL). All tubing was made of Teflon. The total mass flow in the inlet was 2370 sccm. The sample line was 70 cm long with an inner diameter of 6.4 mm. From this flow, Fast O3 sampled 500 sccm through a 140 cm-long line with an inner diameter of 3.8 mm. All flows had at a constant absolute pressure of 70

155 torr. Total residence time is 0.75 s. Fast O3 provides 10 Hz data by detecting photons from the following chemiluminescence reaction:

$$O_3 + NO \rightarrow O_2 + NO_2^*$$ (R1)

$$NO_2^* \rightarrow NO_2 + h\nu$$ (R2)

The excited NO_2 in R2 can also be quenched by collision with other molecules. Water vapor

160 quenches excited NO_2 more efficiently than do nitrogen or oxygen (Matthews et al., 1977), so after time stamp synchronization among the instruments (see Sect. 2.3.), the following water vapor correction is applied (Ridley et al., 1992):

$$[O_3]_{corrected} = [O_3] \times (1 + 4.3(\pm0.3) \times 10^{-3} \times [H_2O])$$ (1)

where [O3] is the ozone mixing ratio in ppbv, and [H2O] is the water vapor mixing ratio in

165 permille by volume of dry air.

The water vapor correction is performed using VCSEL water vapor data (see Sect. 2.2.) that are collected at a higher frequency (25 Hz) than are the Fast O3 data. Thus, the water vapor correction is expected to contribute negligible bias to the EC flux calculations. To assess the potential impact of the water vapor correction on Fast O3 EC fluxes, the constant in eq. (1) was

170 varied from its minimum and maximum estimated values (4.0 – 4.6) in the RF03-C-2 leg; the change in this parameter resulted in biases in the EC flux results of no more than 0.7%. Neglecting the water vapor correction altogether decreased the calculated exchange velocity (see Sect. 2.4) by 5% from 0.131 cm s^{-1} to 0.124 cm s^{-1} (see Table 2). Using the average water vapor concentration during the entire leg for the water vapor correction increases the calculated

175 exchange velocity 2% to 0.134 cm s^{-1}; this case represents the extreme case in which water vapor

reaching the ozone instruments is completely smeared out by longitudinal diffusion. We conclude that water vapor interference in the Fast O3 instrument contributes at most 5% to the ozone flux uncertainty, and likely less than 2%. However, since tThe 0.131 cm s^{-1} value is in good agreement with the EC flux results from FAIRO 1 and FAIRO 2, and since the Fast O3

180 exchange velocities are not systematically higher or lower than those from FAIRO 1 or FAIRO 2, we believe that the water vapor correction is not a source of bias in EC flux calculations. The water vapor interference for the coumarin instruments goes in the opposite direction than for the UV instruments, i.e. water vapor makes Fast O3 less sensitive to ozone, but FAIRO more sensitive (Güsten et al., 1992; Schurath et al., 1991; Zahn et al., 2012). The fact that all three

185 instruments agree after water vapor correction gives us confidence that water vapor bias is removed.

The Fast O3 instrument was calibrated after the campaign using a TECO Model 49i-PS ozone primary standard. The typical instrument detection limit is 0.5 ppbv Hz$^{-0.5}$ with an accuracy not better than 5% at high signal to noise.

190 **2.2.2. The KIT Fast AIRborne Ozone (FAIRO) instruments**

Two identical FAIRO instruments were deployed. The FAIRO instruments were independently checked for proper functioning both prior to the campaign using an Ansyco (now Gasmet Technologies) SYCOS KT-O3M and after the campaign using a TECO 49i-PS. The FAIROs sampled from a separate HIMIL (aft-facing inlet line) through a PFA line with a length of 4.3 m

195 and a 0.42 cm (1/6 in.)1/6-inch inner diameter. Outside air was pulled at 11 vol.-L min^{-1} at ambient pressure by a Vacuubrand MD1 pump downstream of the instruments. Residence time in the line is approximately 0.3 s. The flow was split at a T-fitting ~0.5 m ahead of the FAIROs.

Internally, 2.5 vol.-L min^{-1} of flow went to the UV photometer, which measured ozone absorption around 255 nm within the Hartley band. The O_3 absorption cross section and

200   temperature dependence are taken from (Barnes and Mauersberger, (1987). The UV absorption channel operates at 0.25 Hz. A second, faster 12.5 Hz coumarin chemiluminescence detector (CID) (Ermel et al., 2013) is calibrated against the UV channel and provides the data used in EC flux calculations. The dual detector FAIRO design has two main advantages over the Fast O3 instrument: the FAIROs are lightweight (approx. 14 kg, 19'' rack slot with 3 height units per

205   instrument) and do not require operating fluids such as compressed gases. Scattering by aerosols and absorption by aromatic compounds and water vapor are well-known interferences for UV ozone instruments (Dunlea et al., 2006). The potential for humidity changes to interference with FAIRO uv UV photometers was further investigated, and is found to be small yet not fully insignificant (see Supplementary Figure S1). Interference from aerosols is avoided by the

210   backward-facing sample inlet and aromatic compounds are expected to be minimal in the pristine air sampled in RFs 03-07. A detailed technical description of FAIRO CID can be found in (Zahn et al., (2012). The instrument detection limit is below 1 ppbv Hz$^{-0.5}$ (provided by the CID) and the total uncertainty 1.5% (mainly determined by the uncertainty of the O_3 absorption cross section found in the literature) or 1.5 ppbv, whatever is lower.

215   **2.2. Water vapor: VCSEL**

Water vapor in the free stream above the GV is measured by the vertical cavity surface emitting laser (VCSEL) hygrometer. VCSEL is an open-path optical cavity measuring two absorption lines for high dynamic range: a strong line at 1854.03 nm for low vmrs and a weak line at 1853.37 nm for high vmrs. Data are collected at 25 Hz. During the flux legs, water vapor is

220 always above the VCSEL detection limit of 0.8 ppmv. Details about the operation of VCSEL can

be found in Zondlo et al., (2010).

2.3. Instrument time stamp synchronization

The three ozone instruments and the GV variables are measured on four independent time

stamps, each with its own potential offset and drift. Conveniently, ozone and water vapor vmrs

225 are occasionally anticorrelated (and less frequently, correlated). We use these anticorrelation

events to synchronize each ozone instrument with VCSEL since VCSEL is already synchronized

to the anemometer. First, the ozone and VCSEL signals are interpolated to a common 100 Hz

timestamp. Second, each ozone time series is visually inspected to identify unambiguous

anticorrelation events with the water vapor time series in the periods before and after each flux

230 leg. Third, the time lag at each anticorrelation event is determined by shifting the interpolated

ozone signal until the absolute value of the covariance between the ozone and VCSEL signals is

maximized. Finally, with the time lag identified both before and after the leg, the ozone time

stamp is linearly stretched to match the VCSEL time stamp. Anticorrelation events are not

uncommon. For instrument intercomparison, anticorrelation events from the start and end of the

235 entire flight are used to synchronize data; averaging the synchronized data over 10 s is sufficient

to resolve any residual (<100 ms) synchronization uncertainty. For flux sampling, anticorrelation

events were found before and after each flux leg.

2.4. Eddy covariance flux calculations

Eddy covariance (EC) is a commonly used technique to determine the fluxes of gases in well-

240 mixed surface layers. Given chemical concentration and wind speed data, EC flux can be

calculated as:

$$ECflux = cov(x, w) = \frac{1}{n}\sum_{i=1}^{n}(x_i - \overline{x})(w_i - \overline{w}) \tag{2}$$

where x is the concentration of the chemical species and w is the vertical wind component. For non-stationary conditions, wavelet analysis (WA) is commonly employed instead (Torrence and

245 Compo, 1998). Stationarity is not required for WA because WA decomposes the total flux into component fluxes at different frequencies. In WA, the time series are first transformed into a wavelet by convolution with a wavelet function:

$$W_s(a, b) = \int_{-\infty}^{\infty} s(t)\,\psi_{a,b}(t)dt \tag{3}$$

$$\psi_{a,b}(t) = \frac{1}{\sqrt{a}}\psi_0\left(\frac{t-b}{a}\right) \tag{4}$$

250 where a and b are scale and translation factors for Ψ_0, the "mother wavelet" function. For eddy covariance applications, the typical choice for the mother wavelet is the Morlet wavelet:

$$\psi_0(\eta) = \pi^{\frac{-1}{4}}e^{i\omega_0\eta}e^{\frac{-\eta^2}{2}}, \omega_0 = 6 \tag{5}$$

The WA flux is then calculated as $|W_w W_x|$, where W_w and W_x are the wavelet coefficients of wind and ozone, respectively (Wolfe et al., 2018).

255 A challenge in EC flux error analysis is that EC flux is not a measurement from a single instrument, but rather the combination of measurements from two instruments: a chemical monitor of some sort and an anemometer. For individual instruments, estimation of the limit of detection (LOD) from random error (RE) can be straightforward:

$$LOD = \alpha \times RE \tag{6}$$

260 where α is a dimensionless factor corresponding to the confidence level (1.96 for 95% CL, 3 for 99% CL). The standard deviation of blank measurements can be used to estimate the RE of a single instrument. However, this method is not applicable to flux measurements due to the lack of true "blanks" matching the chemical and meteorological conditions of interest.

Several methods for determining the LOD of EC flux measurements have been put forth based
265 on statistical treatments of the cross-covariance of the chemical and wind data at different time lags. For example, (Langford et al., (2015) present the following formula for estimating the root mean squared error (RE$_{RMSE}$):

$$RE_{RMSE} = \sqrt{0.5\left(\left(\sigma_{f_{w'c'_{[-\Gamma]}}}\right)^2 + \left(\overline{f_{w'c'_{[-\Gamma]}}}\right)^2 + \left(\sigma_{f_{w'c'_{[+\Gamma]}}}\right)^2 + \left(\overline{f_{w'c'_{[+\Gamma]}}}\right)^2\right)} \qquad (7)$$

where $\sigma_{f_{w'c'}}$ and $\overline{f_{w'c'}}$ are the standard deviation and average of the cross-covariance, and $\pm\Gamma$
270 represent time lags far away from the true time lag between the wind and chemical measurements. Currently, no well-established method for estimating the LOD of EC and WA fluxes is commonly accepted. The number of independent replicate measurements of ozone available during TI^{3}GER gave us the unique opportunity to explore, evaluate and optimize methods to constrain the uncertainty of EC fluxes, since the standard deviation of the fluxes
275 measured between the individual instruments can give a sense of the magnitude of the "true" error.

A MATLAB toolkit (AirChem/FluxToolbox: Collections of scripts for eddy covariance flux calculations (both traditional and wavelet-based)., 2023) was used for this work. Raw data must be pre-processed to remove data gaps before inputting to the toolbox. Data gaps are removed by
280 linear interpolation; such gaps are rare, and interpolation is used only to remove up to three or

four points (out of ~2000-4000 which is typical for a flux leg). Because the GV data are recorded at higher resolution than are the ozone data, the wind and VCSEL data are binned to each ozone instrument's corrected time stamp.

For EC fluxes, the toolbox detrends the data with a boxcar method in a user-defined time frame.
285 The lengths of the detrending time frames were selected to balance being short enough to remove systematic cross-covariance structures with being long enough to retain low-frequency fluxes. A detrending time of 10 s was used in all fluxes presented below. For all flux legs, various detrending times were tested to see whether visually identifiable structures could be observed in the cross-covariance. A uniform 10 s detrending time was found to remove systematic structures
290 from all flux legs. To minimize the number of subjective inputs, we did not attempt to customize the detrending time for each flux leg. Because detrending accounts for meteorological conditions rather than instrument response, meaningful intercomparisons could be performed using uniform conditions and consistent detrending times. At typical aircraft speeds, 10 s corresponds to 1-1.2 km. In addition to calculating an eddy covariance flux, the toolbox also calculates WA flux
295 (Torrence and Compo, 1998) and outputs cospectra as a function of frequency.

In contrast to common practice, we express ozone fluxes in terms of exchange velocity (v_e) rather than deposition velocity (v_d), where:

$$v_e = \frac{flux(ppbms^{-1})}{concentration(ppb)} \times \frac{100cm}{1m} \tag{8}$$

Exchange velocity is the same as deposition velocity apart from the lack of a negative sign, i.e.
300 upward directed fluxes have positive v_e. We use v_e rather than v_d because some interesting case studies presented have upward directed fluxes, which are more intuitively represented using positive signs.

Notably, fluxes and cross-covariances in principle have the same units (molec cm^{-2} s^{-1} or ppb m s^{-1}). However, we use "covariance" to refer to the cross-covariance calculated for different lag

305 times by our code, and "flux" to identify an atmospheric state. This distinction is useful when discussing EC flux errors, which are estimated from cross-covariances at time lags departing from the true lag between instruments. Whereas such cross-covariances represent true statistical covariance, they do not represent atmospheric fluxes.

3. Results and Discussion

3.1. Instrument intercomparison

Figure 2 shows the time series of O_3 from all three sensors from RF03 as an example. Panel A

shows the altitude of the GV, and Panel B shows the water vapor and ozone time series for the
entire flight. Water vapor/ozone time synchronization was performed as close to the beginning
and the end of the flight as correlation events could be visually identified; close-ups of these
events are shown in Panels C and E. For EC flux legs, time synchronization was performed
before and after each leg rather than for the entire flight. Because the Fast O3 instrument
computer was not synchronized with the time server, there was an artificial delay of 5 s between
it and VCSEL. After the time synchronization procedure, even artificial clock delays are resolved
to within ±0.1 s.Before the covariance synchronization, the ozone time stamps differed from the
VCSEL time stamp by up to five seconds. The beginning and end close-ups show that the
synchronization procedure matches the signals to within ± 0.1 s. However, Panel D shows that
the ozone signals are not synchronized with each other or to a water vapor correlation event
midway through the flight. The discrepancy could be caused by a combination of different flow
conditions at different altitudes or instrumental clock drift. However, because the FAIRO
instruments share an inlet line that forks only in the last ~0.5 m, inlet line flow differences alone
cannot explain their time offset. Inspection of the delays from each RF show that the ozone
clocks drift no more than ±0.7 s (typically ≤0.5 s). For ozone instrument comparisons, data were
averaged over 10 s to prevent bias from synchronization errors.

Aggregated data from RF03-07 are shown in Figure 3, Panel A. Ozone vmrs measured by each
FAIRO are plotted against ozone vmrs measured by Fast O3. Linear fits of the FAIRO vmrs are

also shown. The data from both instrument designs appear to be linear, with a 2% overall difference. In Panels B-D, the absolute and relative differences between each instrument and the average of all three instruments are shown (see Fig. 3). In all cases, data are color-coded for high water vapor (concentration > 1.4×10^{17} molec cm^{-3}, blue) and high NOx (volume mixing ratio > 200 pptv, red). GPS altitude, VCSEL water vapor concentration, and NOx are also shown in the background of Panels B, C, and D, respectively, for context. Neither the absolute nor the relative differences from the average exhibit systematic behavior depending on water vapor or NOx. The effect of humidity changes did not reveal any obvious explanation for O$_3$ differences when comparing individual instruments to the instrument mean (not shown).; Forfor the effect of changing humidity when comparing FAIRO instruments, see Supplementary Figure S1; for the effect of changing humidity on FAIRO to Fast O3 comparison, see Supplementary Figure S2). Although the persistent differences from average are accompanied by high NOx conditions between ~00:00-02:00 on 21 April 2022 UTC, high NOx conditions between ~19:30-20:00 on 20 April 2022 UTC are not accompanied by similar differences. High water vapor during a low-altitude flux leg at 21:00 UTC is accompanied by agreement amongst all three instruments within 2%.

The agreement of the instruments was also evaluated individually for RFs 03-07. The fit results for each flight are shown in Table 1.

A subset of flux legs with low ozone variability was used to infer an upper limit of the precision of each instrument, as the contribution by additional atmospheric variability can't cannot be fully eliminated. The ozone time series from each flux leg is smoothed over one second and the range is calculated of the smoothed data. Variability is calculated as the relative range of ozone in that

leg. Flux legs are characterized as low-variability if the relative range of the smoothed time series is less than 5% for at least two instruments. Precision is calculated as the standard deviation of the unsmoothed time series. All three instruments have comparable precision, with Fast O3 precision at 1.4% (0.45 ppb) at 10 Hz, FAIRO 1 at 1.2% (0.36 ppb) at 12.5 Hz, and FAIRO 2 at 1.1% (0.36 ppb) at 12.5 Hz. These precision estimates represent an upper bound as some of the variability could be true atmospheric variability. More detail on the precision calculations can be found in Table S2 of the supplement.

3.2. Eddy covariance flux

Potential temperature (Θ) and equivalent potential temperature (Θ_e) profiles are used to determine whether flux legs were conducted within the MBL. Example profiles are shown in Figure 4. The profiles shown are taken from both descent and ascent except in the case of the RF03-C flux legs, which were performed as the plane approached the airport for landing. The flux legs in RF04 were conducted over the tropical Pacific Ocean, and both profiles indicate an MBL height of ~800 m. The utility of Θ_e in determining the MBL height is evident in the RF06-A legs, which were conducted off the coast of Alaska. The Θ profile on the descent does not unambiguously show an MBL height, but the Θ_e profile clearly indicates an MBL height of ~200 m on both the descent and ascent. Such a shallow MBL near the Kenai Fjords combined with the strong temperature inversion suggests RF06-A may be subject to distinct "pools" of air; yet the Θ_e profiles suggest mixing to the surface. The MBL height in RF03-A is difficult to distinguish and may be ~500 m. In all cases, flux legs were conducted at heights well within the MBL except in RF03, where flux legs were conducted at 107, 476, and 889 m.

Whereas the Fast O3 instrument used constant mass flow at constant pressure, the FAIRO instruments used constant volume flow at ambient pressure. In principle, the flow rates in the two instrument designs could differ between the high altitude/low pressure legs typically used for time synchronization and the low altitude/high pressure legs used for flux measurements. Although the different flow rates can create time lag between wind and ozone data, no systematic error is introduced to the ozone flux because we empirically determine the time offset, and do not prescribe a constant offset in the MATLAB flux toolkit. Rather, the time synchronization is used in conjunction with water vapor fluxes calculated from VCSEL data to find the true ozone time offset.

The time delay between VCSEL and the wind data is determined by calculating the water vapor flux. VCSEL and wind speed data are well-synchronized; in most (12) cases, the water vapor cross-covariance had a peak at a time lag of zero points; in six cases the optimal lag was -1 point on the 12.5 Hz FAIRO time stamp (within 0.08 s). In one case (RF07-A-4) the VCSEL cross-covariance peaked at +5 points, but this is likely a spurious correlation because the VCSEL data from the previous leg was well-synchronized (zero time lag). Cross-covariance and cospectra for ozone and water vapor are shown for selected flux legs (RF03-C-2, RF04-A-1, and RF06-A-1) in Figure 5 (see Sect. 3.4).

Because water vapor fluxes are strong and always above detection, the VCSEL/wind time offset allows us to anchor the ozone time offset and limit our search for an ozone covariance peak to ±0.7 s from the VCSEL time offset since that is the maximum observed ozone/VCSEL time delay. An ozone flux is reported for an instrument only if a cross-covariance peak is found within that window. A flux is not reported for an instrument if the covariance behavior within that

window is primarily one of sign-change, e.g. if the covariance linearly increases from negative to positive, or if there are many zero-crossings. If all three instruments show a covariance that survives this filter, then an average flux is reported for that leg. Of the 19 flux legs, 11 had fluxes that met this criterion, and are summarized in Table 2. A full version of Table 2 with

400   meteorological conditions and other compounds of interest is included in the Supplementary Information.

The cospectra in Fig. 5 peak from 0.1-0.2 Hz, indicating that the bulk of the fluxes occur at 5-10 s time scales. These timescales are typical for fluxes in the MBL, and an order of magnitude larger than the mixing time for the Fast O_3 instrument, which for background characterization

405   purposes had zero-air injected from the aircraft inlet. The e-fold rise time was <0.5 s, fast enough not to introduce bias to the flux measurements (see Figure S3 in the SI). Indeed, the cumulative frequency graph (ogive) shows that in the case of RF03-C-2, less than 10% of the total flux is carried on <1 s timescales. Ogives are shown in Figure S4. The residence time in the fast ozone instrument detection volume implied a maximum frequency response of 9 Hz. However, high

410   pass attenuation in the inlet manifold limited the frequency response of the fast O_3 instrument to 3 Hz (Lenschow and Raupach, 1991). The FAIRO instruments were not equipped with zero-air injection at the inlet. However, the residence time in the FAIRO flow is shorter than that in Fast O_3. A calculation of FAIRO inlet manifold indicates attenuation of high frequency signals above 20 Hz, and therefore was not the limiting factor in the FAIRO instrument frequency response.

415   Thus, the FAIRO was more sensitive to high-frequency fluxes than the Fast O_3 instrument.

3.3. Comparison with literature

A previous study has compared ozone EC flux measurements from dry chemiluminescence ozone instruments over grassland (Muller et al., 2010), but to our knowledge no instrument intercomparisons have been performed on board aircraft. Aircraft measurements of ozone flux have been reported before over land (Lenschow et al., 1980; Wolfe et al., 2015, 2018) and over the ocean during PASE (Conley et al., 2011). In the latter, ozone exchange velocities were -0.024 ± 0.014 cm s^{-1}. Larger data sets for marine ozone flux have been produced by ship campaigns. The TexAQS cruise reported ozone exchange velocities as large as -0.81 ± 0.27 cm s^{-1} in coastal channels and -0.034 ± 0.003 cm s^{-1} in offshore areas, and the STRATUS cruise measured -0.009 ± 0.001 cm s^{-1} over open ocean areas (Bariteau et al., 2010; Helmig et al., 2006). All three instruments tested here can detect exchange velocities in the lower range observed in the remote ocean.

3.4. Constraining the error estimate

Figure 5 shows three examples of covariance plots from flux legs that are representative of the range of conditions observed. Ozone plots are shown on the left, and the corresponding plots for VCSEL are shown on the right. For all cross-covariances, the Langford LOD is calculated by using $\Gamma = 30$ s at the beginning and end of the cross-covariance plot, and the Langford 99% CL LOD for Fast O3 is shown as a light gray shading. Panel A (RF03-C-2) is a case in which all three ozone instruments measured an upward directed flux and VCSEL (Panel F) shows water vapor directed downward toward the ocean; this case is described in more detail below. Panel B (RF04-A-1) shows ozone depositing into the ocean and water vapor evaporating out of the ocean. These two cases are examples of EC flux strong enough to be unambiguously identified

by all three ozone instruments, i.e. that each instrument's flux measurement is above the LOD as

440 defined by Langford et al. (2015).

Panel C (RF06-A-1) shows a case in which no ozone instrument derived flux is above the Langford LOD. Viewed in isolation, no instrument's cross-covariance is convincing on its own. However, a small candidate peak can be identified within the ±0.5 s interval.

The average exchange velocity measured by all three instruments in RF06-A-1 is -0.010 cm s^{-1}

445 with a standard deviation of 0.004 cm s^{-1}. The Langford RE$_{RMSE}$ for this leg corresponds to 0.0057-0.0074 cm s^{-1} depending on the instrument and thus overstates the error and LOD. We propose a modification of the Langford approach by restricting the interval Γ by calculating the integral time scale. The integral time scale τ characterizes the period over which covariance persists. We estimate τ by integrating outward from the peak until the integral crosses zero

450 (Lenschow et al., 2000). It is possible in certain cases for the calculation of τ to fail. This happened for the VCSEL data shown in Panel H (RF06-A-1). In this case τ was estimated as the width between the second zero-crossings from the peak.

We then apply the Langford RE$_{RMSE}$ calculation to intervals $+\Gamma$ and $-\Gamma$ which are τ in length and are centered around relatively smooth areas of cross-correlation near the candidate peak.

455 Identifying "smooth" areas was necessarily subjective as the cross-correlation behavior is unique to each leg. The 99% LOD calculated in this modified approach is shown in Figure 5 as dark gray shading. The RE$_{RMSE}$ estimated by the modified approach corresponds to 0.0053-0.0064 cm s^{-1}, which is more in line with the "true" random error among the three measurements.

3.5. Spatial variability of ozone and water vapor fluxes

460   The fluxes of ozone and water vapor were in the counterintuitive directions during the RF03-C

legs. Figure 6 shows profiles, fluxes, and flight movie stills from this leg. Water vapor was

carried downwards, although the ocean surface is usually a water vapor source by evaporation.

Conversely, ozone was carried upwards, even though the ocean surface is expected to be an

ozone sink. The ozone exchange velocity in this leg (RF03-C-2) was +0.134 cm s^{-1} measured at

465   an altitude of 889 m. At a lower altitude of 476 m, (RF03-C-3), the exchange velocity was

+0.097 cm s^{-1}. These velocities are consistent with the lower range of nocturnal entrainment

velocities (0.12 – 0.72 cm s^{-1}) measured during the DYCOMS-II campaign over the Eastern

Pacific Ocean (Faloona et al., 2005).

The entrainment velocity as defined by (Deardorff, (1976) is modified here, as in exchange

470   velocity, such that upward is positive:

$$w_e = \frac{flux(ppbms^{-1})}{\Delta-concentration(ppb)} \times \frac{100cm}{1m} \tag{9}$$

In Equation 9, Δ-concentration is the difference in the concentration of a species across a

boundary to the mixed layer. In previous work, the flux at the transition layer (TL) was

extrapolated from the measured fluxes in stacked legs within the MBL and used to estimate the

475   entrainment velocity (Faloona et al., 2005; Wolfe et al., 2015). This method is not applicable to

the RF03-C legs because the conditions are not mixed to the surface, and because RF03-C-2 is

flown en route to the airport in a decoupled TL characterized by minimum O$_3$ concentrations and

a partial cloud layer near the top (visually estimated from flight videos as ~1 km). The MBL

below extends to ~500m, and the entrainment velocity measured during RF03-C-3 at this altitude

480   (Figure 6, Panel A, shaded) is 6.3 times smaller than the exchange velocity based on the

observed ΔO_3 of 5.2 ppb and Eq. (9) (existence of a concentration change is not necessarily indicative of a flux); the lower O_3 in the decoupled TL is hence curious. Contributions due to entrainment of ozone from the free troposphere would result in a negative exchange velocity during RF03-C-2 (the O_3 profile increases with altitude in the free troposphere) and cannot

485   explain the positive O_3 exchange velocity observed. If there were a significant O_3 entrainment from aloft, the observed positive O_3 exchange velocity would be a lower limit.

Furthermore, the temporal correlation between the O_3 and H_2O fluxes along RF03-C-2 are neither consistent with entrainment from above, nor detrainment from below as a driver of the observed exchange velocities, since the H_2O profile is continuously decreasing with altitude. The

490   negative H_2O flux during RF03-C-2 cannot be explained by entrainment from above or from below. Overhead cloud cover can be qualitatively estimated from NO_2 photolysis frequency (J_{NO2}) measured by the HIAPER Airborne Radiation Package (HARP) actinic flux instrument (Figure 6, Panel B). During cloud-free portions of RF03-C-2 the exchange velocity approaches zero for both H_2O and O_3, indicating that the observed exchange velocities are cloud related.

495   There are only two possible explanations: (1) the cloud induces dynamical change to increase O_3 entrainment from the MBL into the decoupled TL (in which case the H_2O source above the aircraft is a lower limit); or (2) the cloud above is a sink of O_3 and a source of H_2O (evaporating cloud). Notably, the WA time series in Fig. 6 reveals a pronounced maximum O_3 exchange velocity of $+1.8$ cm s^{-1} at the edge of a cloud. Such a large O_3 exchange velocity would require a

500   five-fold larger ΔO_3 towards the MBL than is compatible with the observed O_3 profile, and would require O_3 concentrations in the MBL well in excess of 50 ppbv. No such elevated O_3 concentrations were observed anywhere near this case study, nor during landing (the O_3 concentration two minutes before landing was 32 ppbv, compatible with the profile shown in Fig.

6). Detrainment of O_3 from below, and entrainment of O_3 from the free troposphere hence cannot

505 explain the observed positive O_3 exchange velocity during portions of RF03-C-2. We conclude

that a chemical O_3 sink related to an evaporating cloud is the most likely explanation for our

observations.

However, entrainment cannot explain these fluxes because the air above the plane was dryer, as can be seen from the profiles in Figure 6.

510 A plausible source of water vapor above the plane is evaporating cloud droplets; indeed, footage from this RF shows the plane flying below numerous low clouds. RF03-C took place near solar noon, so the NO_2 photolysis frequency (J_{NO2}) measured by the HIAPER Airborne Radiation Package (HARP) actinic flux instrument can be used as a proxy for overhead cloudiness (see top panel of Figure 6). A period of high ozone and water vapor flux between 22:41 and 22:43 UTC is

515 accompanied by oscillations in J_{NO2} that indicate heavy cloud cover. Stills from the flight movies are shown in Figure 7.

In the left panel of Figure 7, the forward- and side-looking cameras show light high-altitude clouds corresponding to a time (22:39:59 UTC) of low J_{NO2} variability and fluxes near zero for both ozone and water vapor. The right panels show the same views with heavy low clouds

520 visible, corresponding to a time (22:41:57 UTC) when the J_{NO2} variability is high, water vapor flux is toward the ocean, and ozone flux is toward the clouds above.

We hypothesize that evaporating clouds provide a source of water vapor while simultaneously providing a sink of ozone. Previously, it was proposed that an increase in aqueous phase

chemistry in cloud droplets would decrease ozone production in high-NOx environments and

525 enhance ozone destruction in low-NOx environments (Lelieveld and Crutzen, 1990).

Computational simulations suggest that ozone could be stabilized within the air-water interface (within the first 4 Å), and that modification of the ozone UV-vis absorption cross section and activation of photolytic pathways at the interface can increase the ozone photolysis rate constant by more than a factor of 20 (Anglada et al., 2014). The observations from the RF03-C legs may

530   represent the first field evidence of these proposed processes. Critically, the RF03-C-1 flux leg performed at 107 m immediately prior to the RF03-C-2 887 m leg found fluxes below detection for all three ozone instruments. Thus, if cloud effects are operative, they may well be invisible to surface-based platforms such as ships.

Compared to shipborne measurements taken over the course of days or weeks, the flux legs here

535   are necessarily shorter, with the longest leg being ten minutes and the legs being only ~5 minutes long on average. To assess the consistency between sensors on shorter time scales, the ozone EC fluxes were also calculated in 75-second long quarters for the flux example RF06-A-1 shown in Figure 7. The ozone flux observed in this leg is carried in the first, third, and last quarters, with flux in the second quarter below detection. However, the water vapor flux is above detection in

540   all segments and exhibits different trends from the ozone flux. Since the water vapor and ozone are both carried by the same eddies, the difference in behavior cannot be attributed to meteorology. Rather, the ozone flux variability must reflect true heterogeneity in the ocean and/or atmospheric chemical states. Assuming chemical measurements are available on similar time scales, the ozone flux can help characterize atmospheric chemistry on ~10 km spatial scales.

545   For measuring average fluxes, we recommend flying multiple flux legs over regions of interest for better statistics as ozone fluxes are often near the LOD.

4. Conclusions and Outlook

In the aggregate, Fast O3 and FAIRO instruments operate at comparable frequencies (10 vs 12.5 Hz data rate; 3 Hz practical resolution estimated from the mixing time of zero-air puffs at the Fast O3 inlet), are accurate within 2%, and have similar LOD at their typical sampling rates (1.5 ppbv). Large excursions in measured ozone vmrs (of up to 30%, or 5 ppbv difference) are sometimes observed in the ratio of high-rate data between the instruments, but the excursions show no systematic behavior with respect to ozone concentration, water vapor or NOx. These differences did not occur during the flux legs. From an operational standpoint, the FAIRO design is advantageous, because the instrument and pump fit into a single 19" rack and requires no hazardous NO gas.

Simultaneous, high-frequency H_2O measurements in the free stream are essential for synchronizing the O_3 sensors and wind measurements, and provide context to the interpretation of O_3 EC fluxes. Inlet line delays, clock drifts, and small inaccuracies in clock synchronizations lead to time offsets that are difficult to characterize with certainty. Correlation events between water vapor and ozone present direct means for clock synchronization. In principle, an ozone time lag could be prescribed by matching the ozone time stamp to the water vapor time stamp and searching for time lag at which water vapor flux peaks since the water vapor flux is always above detection. In practice, clock drifts still necessitate a search for a cross-covariance peak in the ozone flux, albeit in a constrained time window.

The availability of three ozone instruments during TI[3]GER allowed for the estimation of the "true" LOD of the ozone flux (LOD_{ECflux}) using the standard deviation of the EC fluxes measured by each instrument. We use this information to provide a modified procedure to

estimate error and LOD_{ECflux}: the RE_{RMSE} formula (eq. 7) (Langford et al. 2015) is combined with the concept of "integral time scale" (Lenschow et al., 2000). We find that the "true" LOD_{ECflux} (defined as the 95% CI on the mean EC flux) is overestimated by the EC flux uncertainty on an individual sensor when Γ is a large time window (30 sec, as used in Lenshow et al.). Estimating the RE_{RMSE} over a smaller time window shrinks the RM_{RMSE}, and brings the EC flux uncertainty closer to the "true" error inferred from the EC flux standard deviation of three separate sensors, without underestimating the EC flux error. We find that the integral time scale Γ suitable to estimate error is usually a few seconds, and define it here as Γ found by integrating outward from a candidate covariance peak until the first zero-crossing of the covariance integral. Typical LODs for O_3 exchange velocities are 30-50% lower with shorter Γ, with typical LOD ~ 0.005 cm s^{-1}, limited by spurious covariance peaks that are clearly non-physical as they exceed the believable bounds of instrument synchronization.

Ozone EC fluxes measured from aircraft in the remote MBL can exhibit significant time variability on the order of minutes (6-10 km). A similar variability is not seen in the H_2O EC fluxes. While the H_2O EC fluxes are spatially more homogeneous, and de-facto constant (within 25%), a variability in the O_3 EC fluxes of larger than 600% is observed and highly significant (above 6-σ to below detection) on spatial scales of 20 km. This variability is seen consistently by all three sensors over the open ocean environments probed here. Cloud cover can reverse the direction of the O_3 and H_2O fluxes, indicating a source of water vapor and a sink for O_3 above the aircraft, consistent with webcam images of clouds. The drivers of the horizontal variability in O_3 EC fluxes directed into the ocean on fine spatial scales is currently not well understood, but could relate to changes in overhead cloud cover, as well as possibly variability in ocean and atmospheric states. Future studies are needed, and would benefit from repeat legs, and

measurements of ocean state variables. ~~can reverse the direction of the O_3 and H_2O fluxes, indicating a source of water vapor and a sink for O_3 above the aircraft, consistent with webcam images of clouds. The drivers of the horizontal variability in O_3 EC fluxes directed into the ocean~~

595 ~~on fine spatial scales is currently not well understood, but could relate to changes in overhead cloud cover, as well as possibly variability in ocean and atmospheric states. Future studies are needed, and would benefit from repeat legs, and measurements of ocean state variables.~~

Code Availability

The MATLAB flux toolbox is available at: https://github.com/AirChem/FluxToolbox.

600 **Data Availability**

All data used in this paper can be found on the TI3GER field catalog, which is available at the following URL: https://www.eol.ucar.edu/field_projects/ti3ger.

Author Contributions

RV designed the TI^{3}GER project, and as mission scientist planned and led research flights. RC

605 performed data analysis of the EC fluxes and instrument intercomparison, assisted with instrument calibrations and uninstallation, and led the manuscript preparation. FO and AZ calibrated and deployed the FAIRO instruments and provided the FAIRO data. AF and TC calibrated and deployed the Fast O3 instrument and provided Fast O3 data. AR and CW calibrated the wind measurements and provided GV data. RC and RV wrote the manuscript, with

610 contributions from all co-authors.

Competing Interests

At least one of the (co-)authors is a member of the editorial board of Atmospheric Measurement Techniques.

Acknowledgements

615 Financial support for TI³GER from US National Science Foundation award AGS-2027252 (PI:
R. Volkamer) is gratefully acknowledged. RC and RV thank Glenn Wolfe, Erin Delaria and
Reem Hannun, and Dongwook Kim for helpful discussions. TI³GER was supported by the
National Center for Atmospheric Research, which is a major facility sponsored by the NSF under
Cooperative Agreement no. 1852977. The data were collected using NSF's Lower Atmosphere

620 Observing Facilities, which are managed and operated by NCAR's Earth Observing Laboratory.
The GV aircraft was operated by the National Center for Atmospheric Research (NCAR) Earth
Observing Laboratory's (EOL) Research Aviation Facility (RAF). The NCAR ozone
measurements were funded by NSF Lower Atmosphere Observing Facilities and NSF
NCAR/Facilities programs.

625

References

Altimir, N., Kolari, P., Tuovinen, J.-P., Vesala, T., Bäck, J., Suni, T., Kulmala, M., and Hari, P.:
Foliage surface ozone deposition: a role for surface moisture?, Biogeosciences, 3, 209–228,
630 https://doi.org/10.5194/BG-3-209-2006, 2006.

Anglada, J. M., Martins-Costa, M., Ruiz-López, M. F., and Francisco, J. S.: Spectroscopic
signatures of ozone at the air-water interface and photochemistry implications, Proc Natl
Acad Sci U S A, 111, 11618–11623, https://doi.org/10.1073/pnas.1411727111, 2014.

Bariteau, L., Helmig, D., Fairall, C. W., Hare, J. E., Hueber, J., and Lang, E. K.: Determination
635 of oceanic ozone deposition by ship-borne eddy covariance flux measurements, Atmos
Meas Tech, 3, 441–455, https://doi.org/10.5194/amt-3-441-2010, 2010.

Barnes, J. and Mauersberger, K.: Temperature dependence of the ozone absorption cross section
at the 253.7-nm mercury line, Journal of Geophysical Research: Atmospheres, 92, 14861–
14864, https://doi.org/10.1029/JD092ID12P14861, 1987.

640 Barten, J. G. M., Ganzeveld, L. N., Steeneveld, G. J., Blomquist, B. W., Angot, H., Archer, S. D.,
Bariteau, L., Beck, I., Boyer, M., von der Gathen, P., Helmig, D., Howard, D., Hueber, J.,
Jacobi, H. W., Jokinen, T., Laurila, T., Posman, K. M., Quéléver, L., Schmale, J., Shupe, M.

D., and Krol, M. C.: Low ozone dry deposition rates to sea ice during the MOSAiC field campaign: Implications for the Arctic boundary layer ozone budget, Elementa, 11, https://doi.org/10.1525/ELEMENTA.2022.00086/195276, 2023.

Bauer, M. R., Hultman, N. E., Panek, J. A., and Goldstein, A. H.: Ozone deposition to a ponderosa pine plantation in the Sierra Nevada Mountains (CA): A comparison of two different climatic years, Journal of Geophysical Research: Atmospheres, 105, 22123–22136, https://doi.org/10.1029/2000JD900168, 2000.

Boylan, P., Helmig, D., and Park, J. H.: Characterization and mitigation of water vapor effects in the measurement of ozone by chemiluminescence with nitric oxide, Atmos Meas Tech, 7, 1231–1244, https://doi.org/10.5194/AMT-7-1231-2014, 2014.

Chiu, R., Tinel, L., Gonzalez, L., Ciuraru, R., Bernard, F., George, C., and Volkamer, R.: UV photochemistry of carboxylic acids at the air-sea boundary: A relevant source of glyoxal and other oxygenated VOC in the marine atmosphere, Geophys Res Lett, 44, 1079–1087, https://doi.org/10.1002/2016GL071240, 2017.

Clifton, O. E., Fiore, A. M., Massman, W. J., Baublitz, C. B., Coyle, M., Emberson, L., Fares, S., Farmer, D. K., Gentine, P., Gerosa, G., Guenther, A. B., Helmig, D., Lombardozzi, D. L., Munger, J. W., Patton, E. G., Pusede, S. E., Schwede, D. B., Silva, S. J., Sörgel, M., Steiner, A. L., and Tai, A. P. K.: Dry Deposition of Ozone Over Land: Processes, Measurement, and Modeling, Reviews of Geophysics, 58, e2019RG000670, https://doi.org/10.1029/2019RG000670, 2020.

Conley, S. A., Faloona, I. C., Lenschow, D. H., Campos, T., Heizer, C., Weinheimer, A., Cantrell, C. A., Mauldin, R. L., Hornbrook, R. S., Pollack, I., and Bandy, A.: A complete dynamical ozone budget measured in the tropical marine boundary layer during PASE, J Atmos Chem, 68, 55–70, https://doi.org/10.1007/s10874-011-9195-0, 2011.

Deardorff, J. W.: On the entrainment rate of a stratocumulus-topped mixed layer, Quarterly Journal of the Royal Meteorological Society, 102, 563–582, https://doi.org/10.1002/QJ.49710243306, 1976.

Dunlea, E. J., Herndon, S. C., Nelson, D. D., Volkamer, R. M., Lamb, B. K., Allwine, E. J., Grutter, M., Ramos Villegas, C. R., Marquez, C., Blanco, S., Cardenas, B., Kolb, C. E., Molina, L. T., and Molina, M. J.: Technical note: Evaluation of standard ultraviolet absorption ozone monitors in a polluted urban environment, Atmos. Chem. Phys, 6, 3163–3180, 2006.

El-Madany, T. S., Niklasch, K., and Klemm, O.: Stomatal and Non-Stomatal Turbulent Deposition Flux of Ozone to a Managed Peatland, Atmosphere 2017, Vol. 8, Page 175, 8, 175, https://doi.org/10.3390/ATMOS8090175, 2017.

Ermel, M., Oswald, R., Mayer, J. C., Moravek, A., Song, G., Beck, M., Meixner, F. X., and Trebs, I.: Preparation methods to optimize the performance of sensor discs for fast

680   chemiluminescence ozone analyzers, Environ Sci Technol, 47, 1930–1936, https://doi.org/10.1021/ES3040363/SUPPL_FILE/ES3040363_SI_001.PDF, 2013.

Faloona, I., Lenschow, D. H., Campos, T., Stevens, B., van Zanten, M., Blomquist, B., Thornton, D., Bandy, A., and Gerber, H.: Observations of Entrainment in Eastern Pacific Marine Stratocumulus Using Three Conserved Scalars, J Atmos Sci, 62, 3268–3285, https://doi.org/10.1175/JAS3541.1, 2005.

Fares, S., Savi, F., Muller, J., Matteucci, G., and Paoletti, E.: Simultaneous measurements of above and below canopy ozone fluxes help partitioning ozone deposition between its various sinks in a Mediterranean Oak Forest, Agric For Meteorol, 198–199, 181–191, https://doi.org/10.1016/J.AGRFORMET.2014.08.014, 2014.

690 Finco, A., Marzuoli, R., Chiesa, M., and Gerosa, G.: Ozone risk assessment for an Alpine larch forest in two vegetative seasons with different approaches: comparison of POD1 and AOT40, Environmental Science and Pollution Research, 24, 26238–26248, https://doi.org/10.1007/S11356-017-9301-1/FIGURES/6, 2017.

Gallagher, M. W., Beswick, K. M., and Coe, H.: Ozone deposition to coastal waters, Quarterly Journal of the Royal Meteorological Society, 127, 539–558, https://doi.org/10.1002/QJ.49712757215, 2001.

Ganzeveld, L., Helmig, D., Fairall, C. W., Hare, J., and Pozzer, A.: Atmosphere-ocean ozone exchange: A global modeling study of biogeochemical, atmospheric, and waterside turbulence dependencies, Global Biogeochem. Cycles, 23, 4021, https://doi.org/10.1029/2008GB003301, 2009.

Güsten, H. and Heinrich, G.: On-line measurements of ozone surface fluxes: Part I. Methodology and instrumentation, Atmos Environ, 30, 897–909, https://doi.org/10.1016/1352-2310(95)00269-3, 1996.

Güsten, H., Heinrich, G., Schmidt, R. W. H., and Schurath, U.: A novel ozone sensor for direct eddy flux measurements, J Atmos Chem, 14, 73–84, https://doi.org/10.1007/BF00115224/METRICS, 1992.

Güsten, H., Heinrich, G., Mönnich, E., Sprung, D., Weppner, J., Ramadan, A. B., Ezz El-Din, M. R. M., Ahmed, D. M., and Hassan, G. K. Y.: On-line measurements of ozone surface fluxes: Part II. Surface-level ozone fluxes onto the Sahara desert, Atmos Environ, 30, 911–918, https://doi.org/10.1016/1352-2310(95)00270-7, 1996.

Hannun, R. A., Swanson, A. K., Bailey, S. A., Hanisco, T. F., Paul Bui, T., Bourgeois, I., Peischl, J., and Ryerson, T. B.: A cavity-enhanced ultraviolet absorption instrument for high-precision, fast-Time-response ozone measurements, Atmos Meas Tech, 13, 6877–6887, https://doi.org/10.5194/AMT-13-6877-2020, 2020.

715 Helmig, D., Lang, E. K., Bariteau, L., Boylan, P., Fairall, C. W., Ganzeveld, L., Hare, J. E., Hueber, J., and Pallandt, M.: Atmosphere-ocean ozone fluxes during the TexAQS 2006,

STRATUS 2006, GOMECC 2007, GasEx 2008, and AMMA 2008 cruises, Journal of Geophysical Research: Atmospheres, 117, https://doi.org/10.1029/2011JD015955, 2006.

Juráň, S., Šigut, L., Holub, P., Fares, S., Klem, K., Grace, J., and Urban, O.: Ozone flux and ozone deposition in a mountain spruce forest are modulated by sky conditions, Science of The Total Environment, 672, 296–304, https://doi.org/10.1016/J.SCITOTENV.2019.03.491, 2019.

Kammer, J., Lamaud, E., Bonnefond, J. M., Garrigou, D., Flaud, P. M., Perraudin, E., and Villenave, E.: Ozone production in a maritime pine forest in water-stressed conditions, Atmos Environ, 197, 131–140, https://doi.org/10.1016/J.ATMOSENV.2018.10.021, 2019.

Lamaud, E., Carrara, A., Brunet, Y., Lopez, A., and Druilhet, A.: Ozone fluxes above and within a pine forest canopy in dry and wet conditions, Atmos Environ, 36, 77–88, https://doi.org/10.1016/S1352-2310(01)00468-X, 2002.

Lamaud, E., Loubet, B., Irvine, M., Stella, P., Personne, E., and Cellier, P.: Partitioning of ozone deposition over a developed maize crop between stomatal and non-stomatal uptakes, using eddy-covariance flux measurements and modelling, Agric For Meteorol, 149, 1385–1396, https://doi.org/10.1016/J.AGRFORMET.2009.03.017, 2009.

Langford, B., Acton, W., Ammann, C., Valach, A., and Nemitz, E.: Eddy-covariance data with low signal-to-noise ratio: Time-lag determination, uncertainties and limit of detection, Atmos Meas Tech, 8, 4197–4213, https://doi.org/10.5194/AMT-8-4197-2015, 2015.

Lelieveld, J. and Crutzen, P. J.: Influences of cloud photochemical processes on tropospheric ozone, Nature, 343, 227–233, https://doi.org/10.1038/343227a0, 1990.

Lenschow, D. H. and Raupach, M. R.: The attenuation of fluctuations in scalar concentrations through sampling tubes, J Geophys Res, 96, 15259–15268, https://doi.org/10.1029/91JD01437, 1991.

Lenschow, D. H., Delany, A. C., Stankov, B. B., and Stedman, D. H.: Airborne measurements of the vertical flux of ozone in the boundary layer, Boundary Layer Meteorol, 19, 249–265, https://doi.org/10.1007/BF00117223/METRICS, 1980.

Lenschow, D. H., Wulfmeyer, V., and Senff, C.: Measuring Second-through Fourth-Order Moments in Noisy Data, J Atmos Ocean Technol, 17, 1330–1347, https://doi.org/https://doi.org/10.1175/1520-0426(2000)017<1330:MSTFOM>2.0.CO;2, 2000.

Loubet, B., Cellier, P., Fléchard, C., Zurfluh, O., Irvine, M., Lamaud, E., Stella, P., Roche, R., Durand, B., Flura, D., Masson, S., Laville, P., Garrigou, D., Personne, E., Chelle, M., and Castell, J. F.: Investigating discrepancies in heat, CO2 fluxes and O3 deposition velocity over maize as measured by the eddy-covariance and the aerodynamic gradient methods, Agric For Meteorol, 169, 35–50, https://doi.org/10.1016/J.AGRFORMET.2012.09.010, 2013.

Massman, W. J., Macpherson, J. I., Delany, A., Den Hartog, G., Neumann, H. H., Oncley, S. P.,
755   Pearson, R., Pederson, J., and Shaw, R. H.: Surface conductances for ozone uptake derived
from aircraft eddy correlation data, Atmos Environ, 29, 3181–3188,
https://doi.org/10.1016/1352-2310(94)00330-N, 1995.

Matthews, R. D., Sawyer, R. F., and Schefer, R. W.: Interferences in chemiluminescent
measurement of nitric oxide and nitrogen dioxide emissions from combustion systems,
760   Environ Sci Technol, 11, 1092–1096, https://doi.org/10.1021/es60135a005, 1977.

Muller, J. B. A., Coyle, M., Fowler, D., Gallagher, M. W., Nemitz, E. G., and Perciva, C. J.:
Comparison of ozone fluxes over grassland by gradient and eddy covariance technique,
Atmospheric Science Letters, 10, 164–169, https://doi.org/10.1002/ASL.226, 2009.

Muller, J. B. A., Percival, C. J., Gallagher, M. W., Fowler, D., Coyle, M., and Nemitz, E.:
765   Sources of uncertainty in eddy covariance ozone flux measurements made by dry
chemiluminescence fast response analysers, Atmos Meas Tech, 3, 163–176,
https://doi.org/10.5194/AMT-3-163-2010, 2010.

Muller, J. B. A., Dorsey, J. R., Flynn, M., Gallagher, M. W., Percival, C. J., Shallcross, D. E.,
Archibald, A., Roscoe, H. K., Obbard, R. W., Atkinson, H. M., Lee, J. D., Moller, S. J., and
770   Carpenter, L. J.: Energy and ozone fluxes over sea ice, Atmos Environ, 47, 218–225,
https://doi.org/10.1016/J.ATMOSENV.2011.11.013, 2012.

Pearson, R., Jr. and Stedman, D.: Instrumentation for fast-response ozone measurements from
aircraft, Atmos. Technol., 12, 51–54, 1980.

Plake, D., Stella, P., Moravek, A., Mayer, J. C., Ammann, C., Held, A., and Trebs, I.: Comparison
775   of ozone deposition measured with the dynamic chamber and the eddy covariance method,
Agric For Meteorol, 206, 97–112, https://doi.org/10.1016/J.AGRFORMET.2015.02.014,
2015.

Rannik, Ü., Altimir, N., Mammarella, I., Bäck, J., Rinne, J., Ruuskanen, T. M., Hari, P., Vesala,
T., and Kulmala, M.: Ozone deposition into a boreal forest over a decade of observations:
780   Evaluating deposition partitioning and driving variables, Atmos Chem Phys, 12, 12165–
12182, https://doi.org/10.5194/ACP-12-12165-2012, 2012.

Ridley, B. A. and Howlett, L. C.: An instrument for nitric oxide measurements in the
stratosphere, Review of Scientific Instruments, 45, 742–746,
https://doi.org/10.1063/1.1686726, 1974.

785   Ridley, B. A., Schiff, H. I., and Welge, K. H.: Measurement of NO in the Stratosphere by NO/O3
Chemiluminescence (COM-72-10476), 1972.

Ridley, B. A., Grahek, F. E., and Walega, J. G.: A Small High-Sensitivity, Medium-Response
Ozone Detector Suitable for Measurements from Light Aircraft, J Atmos Ocean Technol, 9,
142–148, https://doi.org/https://doi.org/10.1175/1520-
790   0426(1992)009%3C0142:ASHSMR%3E2.0.CO;2, 1992.

Rolph, G., Stein, A., and Stunder, B.: Real-time Environmental Applications and Display sYstem: READY, Environmental Modelling & Software, 95, 210–228, https://doi.org/10.1016/J.ENVSOFT.2017.06.025, 2017.

795 Saiz-Lopez, A., Plane, J. M. C. C., Baker, A. R., Carpenter, L. J., von Glasow, R., Gómez Martín, J. C., McFiggans, G., and Saunders, R. W.: Atmospheric Chemistry of Iodine, Chem Rev, 112, 1773–1804, https://doi.org/10.1021/cr200029u, 2012.

Schurath, U., Speuser, W., and Schmidt, R.: Principle and application of a fast sensor for atmospheric ozone, Fresenius J Anal Chem, 340, 544–547, https://doi.org/10.1007/BF00322426/METRICS, 1991.

800 Stein, A. F., Draxler, R. R., Rolph, G. D., Stunder, B. J. B., Cohen, M. D., and Ngan, F.: NOAA's HYSPLIT Atmospheric Transport and Dispersion Modeling System, Bull Am Meteorol Soc, 96, 2059–2077, https://doi.org/10.1175/BAMS-D-14-00110.1, 2015.

Stella, P., Loubet, B., Lamaud, E., Laville, P., and Cellier, P.: Ozone deposition onto bare soil: A new parameterisation, Agric For Meteorol, 151, 669–681,
805 https://doi.org/10.1016/J.AGRFORMET.2011.01.015, 2011.

Torrence, C. and Compo, G. P.: A Practical Guide to Wavelet Analysis, Bull Am Meteorol Soc, 79, 61–78, https://doi.org/10.1175/1520-0477(1998)079<0061:APGTWA>2.0.CO;2, 1998.

Vermeuel, M. P., Cleary, P. A., Desai, A. R., and Bertram, T. H.: Simultaneous Measurements of O3 and HCOOH Vertical Fluxes Indicate Rapid In-Canopy Terpene Chemistry Enhances
810 O3 Removal Over Mixed Temperate Forests, Geophys Res Lett, 48, e2020GL090996, https://doi.org/10.1029/2020GL090996, 2021.

Wohlfahrt, G., Hörtnagl, L., Hammerle, A., Graus, M., and Hansel, A.: Measuring eddy covariance fluxes of ozone with a slow-response analyser, Atmos Environ, 43, 4570–4576, https://doi.org/10.1016/J.ATMOSENV.2009.06.031, 2009.

815 Wolfe, G. M.: AirChem/FluxToolbox: Collections of scripts for eddy covariance flux calculations (both traditional and wavelet-based).: https://github.com/AirChem/FluxToolbox, last access: 18 May 2023.

Wolfe, G. M., Hanisco, T. F., Arkinson, H. L., Bui, T. P., Crounse, J. D., Dean-Day, J., Goldstein, A., Guenther, A., Hall, S. R., Huey, G., Jacob, D. J., Karl, T., Kim, P. S., Liu, X., Marvin,
820 M. R., Mikoviny, T., Misztal, P. K., Nguyen, T. B., Peischl, J., Pollack, I., Ryerson, T., St. Clair, J. M., Teng, A., Travis, K. R., Ullmann, K., Wennberg, P. O., and Wisthaler, A.: Quantifying sources and sinks of reactive gases in the lower atmosphere using airborne flux observations, Geophys Res Lett, 42, 8231–8240, https://doi.org/10.1002/2015GL065839, 2015.

825 Wolfe, G. M., Kawa, S. R., Hanisco, T. F., Hannun, R. A., Newman, P. A., Swanson, A., Bailey, S., Barrick, J., Thornhill, K. L., Diskin, G., DiGangi, J., Nowak, J. B., Sorenson, C., Bland, G., Yungel, J. K., and Swenson, C. A.: The NASA Carbon Airborne Flux Experiment

(CARAFE): Instrumentation and methodology, Atmos Meas Tech, 11, 1757–1776, https://doi.org/10.5194/amt-11-1757-2018, 2018.

830 Zahn, A., Weppner, J., Widmann, H., Schlote-Holubek, K., Burger, B., K ¨ Uhner, T., and Franke, H.: A fast and precise chemiluminescence ozone detector for eddy flux and airborne application, Atmos. Meas. Tech, 5, 363–375, https://doi.org/10.5194/amt-5-363-2012, 2012.

Zeller, K.: Summer and autumn ozone fluxes to a forest in the Czech Republic Brdy Mountains,
835 Environmental Pollution, 119, 269–278, https://doi.org/10.1016/S0269-7491(01)00176-2, 2002.

Zeller, K. F. and Nikolov, N. T.: Quantifying simultaneous fluxes of ozone, carbon dioxide and water vapor above a subalpine forest ecosystem, Environmental Pollution, 107, 1–20, https://doi.org/10.1016/S0269-7491(99)00156-6, 2000.

840 Zhu, Z., Zhao, F., Voss, L., Xu, L., Sun, X., Yu, G., and Meixner, F. X.: The effects of different calibration and frequency response correction methods on eddy covariance ozone flux measured with a dry chemiluminescence analyzer, Agric For Meteorol, 213, 114–125, https://doi.org/10.1016/J.AGRFORMET.2015.06.016, 2015.

Zhu, Z., Tang, X., and Zhao, F.: Comparison of Ozone Fluxes over a Maize Field Measured with
845 Gradient Methods and the Eddy Covariance Technique, Adv Atmos Sci, 37, 586–596, https://doi.org/https://doi.org/10.1007/s00376-020-9217-4, 2020.

Zhu, Z. L., Sun, X. M., Dong, Y. S., Zhao, F. H., and Meixner, F. X.: Diurnal variation of ozone flux over corn field in Northwestern Shandong Plain of China, Sci China Earth Sci, 57, 503–511, https://doi.org/10.1007/S11430-013-4797-9/METRICS, 2014.

850 Zondlo, M. A., Paige, M. E., Massick, S. M., and Silver, J. A.: Vertical cavity laser hygrometer for the National Science Foundation Gulfstream-V aircraft, Journal of Geophysical Research Atmospheres, 115, https://doi.org/10.1029/2010JD014445, 2010.
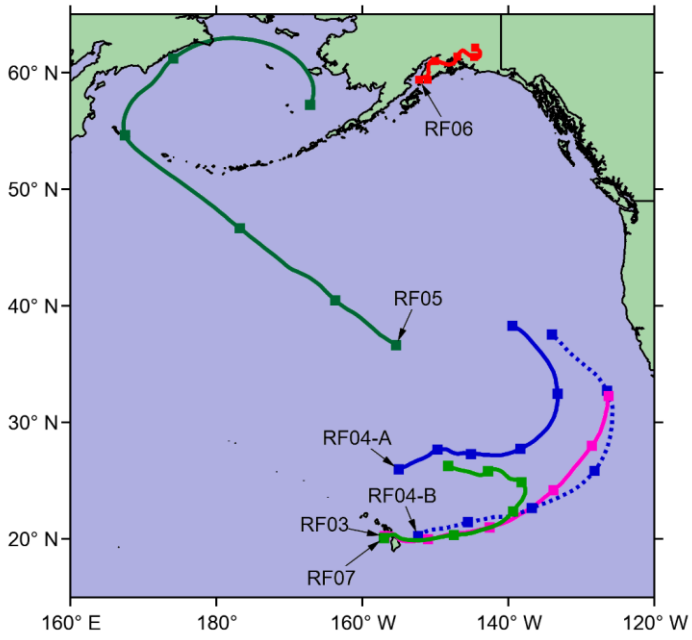
855   Figure 1. Map of flux legs and back-trajectories during TI³GER. Square markers indicate 24-hour periods, and the

arrows mark the location of the flux legs.
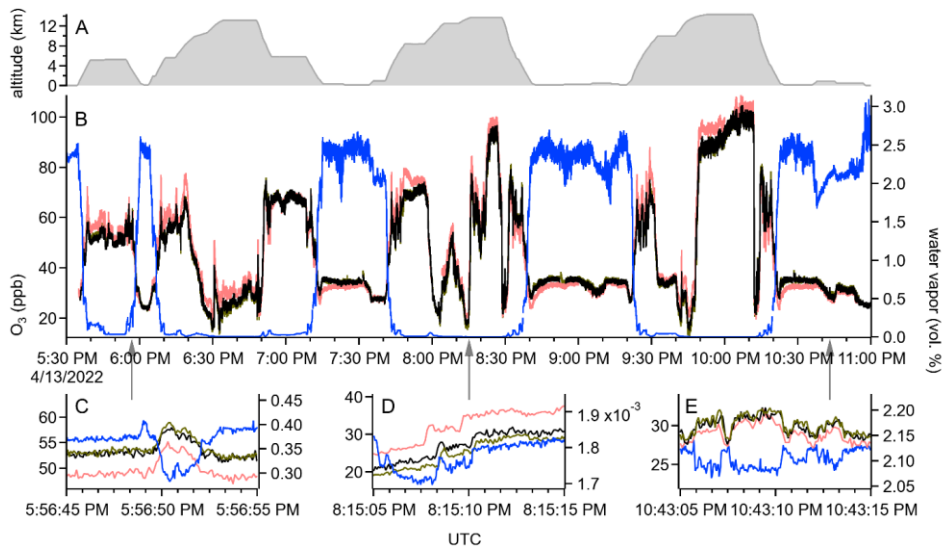
Figure 2. Time stamp synchronization based on the H₂O and O₃ time series. VCSEL data are shown in blue, Fast O3 data in salmon, FAIRO 1 in black, and FAIRO 2 in dark olive. All traces are shown at the native instrument resolution (25 Hz for VCSEL, 12.5 Hz for the FAIROs, and 10 Hz for Fast O3). A: altitude time series. B: time series for the entire flight. C-E: Zooms to cross-covariance events with gray arrows pointing to exact times.

860
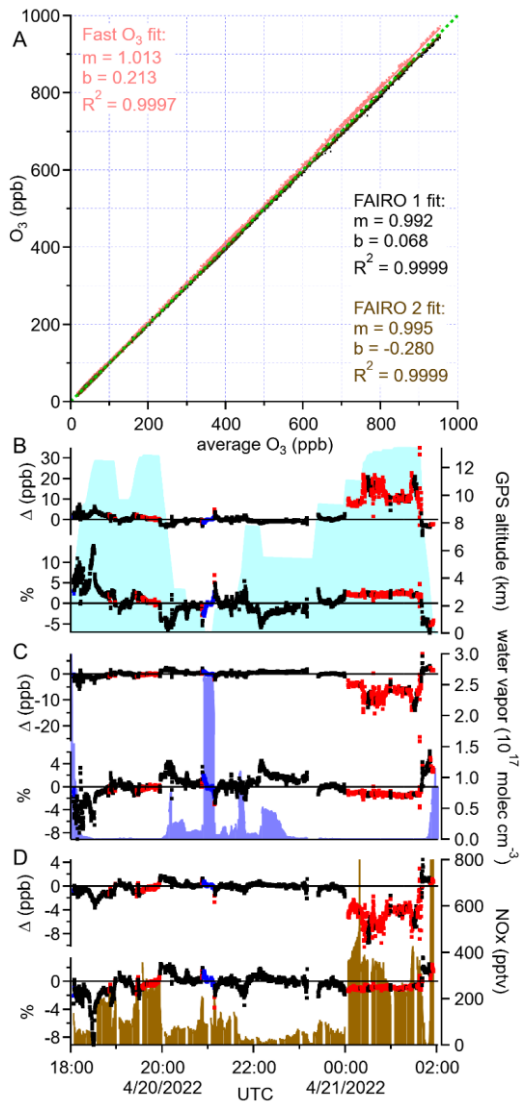
Figure 3. A: Aggregated data from RF03-07 with fits relative to global average; one-to-one line in green. Absolute and relative differences from average during RF05 for Fast O3 in Panel B; FAIRO 1 in Panel C; and FAIRO 2 in Panel D. Background shading for GPS altitude in Panel B, VCSEL in Panel C, and NOx in Panel D.
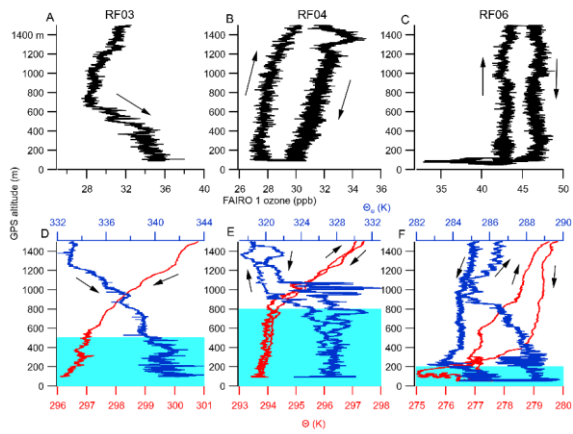
Figure 4. A-C: Profiles of ozone during RF03-C, RF04-A, and RF06-A, respectively. D-F: Corresponding potential temperature and equivalent potential temperature profiles for RF03-C, RF04-A, and RF06-A, respectively. MBL height is shown as light blue shading. Arrows indicate profile ascents and descents. ~~Representative potential temperature and equivalent potential temperature profiles for determining MBL height in three different flux legs. The MBL is shown as light blue shading.~~
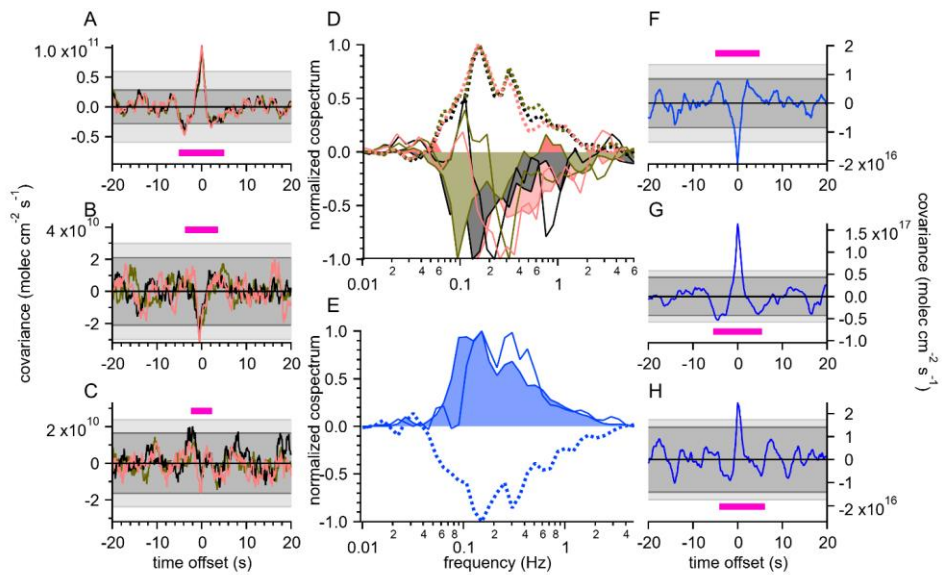
Figure 5. Cross-covariance plots for RF03-C-2 (A), RF04-A-1 (B), and RF06-A-1 (C), and their respective water vapor fluxes (F-H). Normalized cospectra are shown in D and E. Detrending the data at 10 s removes spectral power and frequencies below 0.1 Hz. For ozone data, Fast O3 is shown in salmon, FAIRO 1 in black, and FAIRO 2 in olive. In Panels D and E, RF03 is shown as a dotted line, RF04 as a shade to zero, and RF06 as a solid line. Integral time scales are shown as fuchsia bars.

875
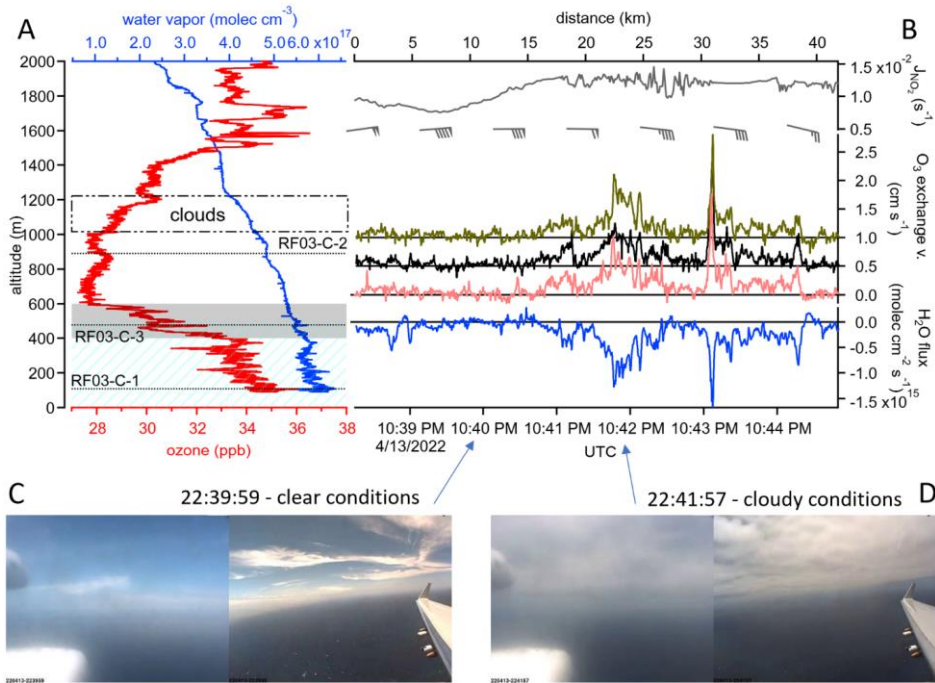
Figure 6. Ozone and water vapor vertical profiles and time series for EC fluxes from the RF03-C leg. Ozone profile is the average of all three instruments. Dashed lines indicate flight altitudes; dashed rectangle represents visually estimated cloud layer. Right: J_{NO2} in gray, fluxes from Fast O3 (salmon), FAIRO 1 (black), FAIRO 2 (olive), and VCSEL (blue). Vertical offsets of 0.5 cm s^{-1} and 1 cm s^{-1} have been added to FAIRO 1 and 2 to better illustrate the close agreement between the three O_3 instruments. Images of the webcams from RF03 flight movies illustrate cloud cover conditions.

880

885
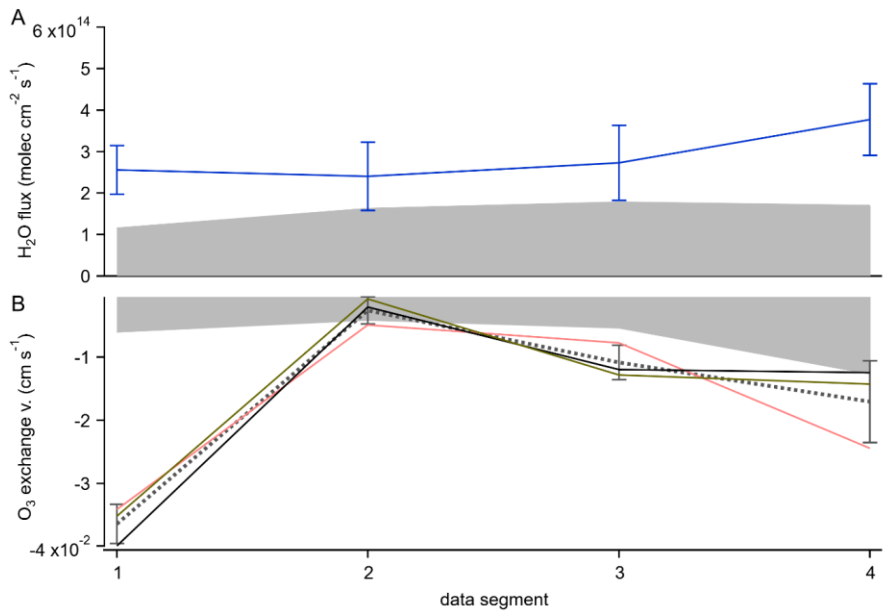
Figure 7. Segments of RF06-A-1. Panel A: VCSEL is shown in blue. Error bars represent modified Langford RE$_{RMSE}$. Panel B: FO3 in salmon, FAIRO 1 in black, and FAIRO 2 in dark olive. The average is shown as the dotted line. Error bars represent standard deviation. In both panels, the 95% LOD is shaded. Each data segment is 75 seconds long.

flight	average (ppb)	max (ppb)	FO3 slope	FO3 offset (ppb)	F1 slope	F1 offset (ppb)	F2 slope	F2 offset (ppb)
RF03	**47.4**	**103**	1.028	0.44	0.982	0.02	0.990	-0.46
RF04	**76.5**	**409**	1.029	-0.03	0.981	0.24	0.989	-0.21
RF05	**172.8**	**955**	1.024	-1.40	0.985	1.10	0.991	0.34
RF06	**223.0**	**887**	1.000	0.15	0.998	0.15	0.998	-0.30
RF07	**78.6**	**177**	1.014	0.08	0.992	-0.04	0.994	-0.04

Table 1. Linear fit parameters of individual instruments to average.

890

Leg Code	Date UTC	Start UTC	End UTC	location	alt (m)	exchange velocity (cm s^{-1})				
						Fast O3	FAIRO 1	FAIRO 2	average	st. dev.
RF03-A-1	4/13/2022	19:16:43	19:20:13	off SW coast of HI	312	+0.037	+0.020	+0.015	+0.024	0.012
RF03-B-1	4/13/2022	20:45:33	20:52:08	off SW coast of HI	101	+0.033	+0.014	+0.003	+0.017	0.015
RF03-C-2	4/13/2022	22:38:15	22:44:51	off SW coast of HI	889	+0.131	+0.135	+0.136	+0.134	0.003
RF03-C-3	4/13/2022	22:46:02	22:54:15	off SW coast of HI	476	+0.099	+0.093	+0.100	+0.097	0.004
RF04-A-1	4/15/2022	21:16:20	21:21:46	North of HI	93	-0.042	-0.037	-0.030	-0.036	0.006
RF04-A-2	4/15/2022	21:22:12	21:25:50	North of HI	101	-0.030	-0.014	-0.017	-0.021	0.008
RF06-A-1	4/21/2022	19:39:47	19:44:44	off AK coast	58	-0.015	-0.008	-0.009	-0.010	0.004
RF06-B-1	4/22/2022	02:28:59	02:32:01	halfway between AK and HI	116	+0.022	+0.024	+0.024	+0.023	0.001
RF07-A-1	4/23/2022	21:43:30	21:49:20	west of HI airport	116	-0.017	-0.013	-0.014	-0.015	0.002
RF07-A-3	4/23/2022	22:04:07	22:06:45	west of HI airport	778	-0.012	-0.015	-0.015	-0.014	0.002
RF07-A-4	4/23/2022	22:11:24	22:16:08	west of HI airport	472	-0.035	-0.029	-0.036	-0.033	0.004

Table 2. Summary of ozone EC flux results.